

Temperature and acoustic impedance simultaneous sensor based on forward stimulated Brillouin scattering in highly nonlinear fiber

Shilong Liu(刘仕龙), Yang Li(李阳), Hongbin Hu(胡洪彬), Bing Sun(孙兵), and Zuxing Zhang(张祖兴)
Citation: Chin. Phys. B, 2025, 34 (**7**): 074212. DOI: 10.1088/1674-1056/adca1b
http://cpb.iphy.ac.cn; http://iopscience.iop.org/cpb

What follows is a list of articles you may be interested in

Simultaneous measurements of refractive index and temperature based on a no-core fiber coated with Ag and PDMS films

Yuxin Li(李宇昕), Hailiang Chen(陈海良), Yingyue Zhang(张赢月), Qiang Chen(陈强), Biao Wu(武彪),Xiaoya Fan(樊晓亚), Yingchao Liu(刘英超), and Mingjian Ma(马明建)
Chin. Phys. B, 2023, 32 (**5**): 054209. DOI: 10.1088/1674-1056/ac8f36

High sensitivity plasmonic temperature sensor based on a side-polished photonic crystal fiber

Zhigang Gao(高治刚), Xili Jing(井西利), Yundong Liu(刘云东), Hailiang Chen(陈海良), and Shuguang Li(李曙光)
Chin. Phys. B, 2022, 31 (**2**): 024207. DOI: 10.1088/1674-1056/ac0a63

Highly sensitive optical fiber temperature sensor based on resonance in sidewall of liquid-filled silica capillary tube

Min Li(李敏), Biao Feng(冯彪), Jiwen Yin(尹辑文)
Chin. Phys. B, 2019, 28 (**11**): 114201. DOI: 10.1088/1674-1056/ab43be

Multi-functional optical fiber sensor system based ona dense wavelength division multiplexer

Yue-Xin Yin(尹悦鑫), Zhifa Wu(吴志发), Siwen Sun(孙思文), Liang Tian(田亮), Xibin Wang(王希斌), Yuanda Wu(吴远大), Daming Zhang(张大明)
Chin. Phys. B, 2019, 28 (**7**): 074202. DOI: 10.1088/1674-1056/28/7/074202

Temperature dependence of the refractive index of optical fibers

Wang Zhi-Yong (王智勇), Qiu Qi (邱琪), Shi Shuang-Jin (史双瑾)
Chin. Phys. B, 2014, 23 (**3**): 034201. DOI: 10.1088/1674-1056/23/3/034201

Temperature and acoustic impedance simultaneous sensor based on forward stimulated Brillouin scattering in highly nonlinear fiber

Shilong Liu(刘仕龙), Yang Li(李阳), Hongbin Hu(胡洪彬), Bing Sun(孙兵), and Zuxing Zhang(张祖兴)†

Advanced Photonic Technology Laboratory, the College of Electronic and Optical Engineering, Nanjing University of Posts and Telecommunications, Nanjing 210023, *China*

(Received 24 February 2025; revised manuscript received 28 March 2025; accepted manuscript online 8 April 2025)

A temperature and acoustic impedance simultaneous sensor based on forward stimulated Brillouin scattering (FSBS) in highly nonlinear fiber (HNLF) with high sensitivity and high accuracy is proposed and demonstrated in this paper. High-order acoustic modes (HOAMs) are used to achieve individual or simultaneous measurement of the two parameters. Transverse acoustic waves (TAWs) involved in the FSBS process can efficiently sense the mechanical or environmental changes outside the fiber cladding, which will be reflected in a linear shift of the acoustic resonance frequency. By analyzing the frequencies of specific scattering peaks, the temperature and acoustic impedance outside the fiber cladding can be obtained simultaneously. The highest measured temperature and acoustic impedance sensitivities are 184.93 kHz/°C and 444.56 kHz/MRayl, and the measurement accuracies are 0.09 °C and 0.009 MRayl, respectively, which are both at desirable levels. We believe this work can provide potential application solutions for sensing fields involving temperature or acoustic impedance measurements.

Keywords: forward stimulated Brillouin scattering (FSBS), fiber optic sensor, temperature sensor, acoustic impedance sensor, simultaneous measurement

PACS: 42.81.Pa, 42.81.–i, 07.07.Df

DOI: 10.1088/1674-1056/adca1b **CSTR:** 32038.14.CPB.adca1b

1. Introduction

Fiber-optic sensors are widely used in plenty of academic fields involving physical, chemical and biological elements due to their advantages such as small size, light weight, and high resistance to electromagnetic interference.[1,2] In particular, individual or simultaneous sensing techniques for temperature and acoustic impedance have been one of the research favorites in these fields,[3,4] and they are valuable in various scenarios such as oil and gas energy production and transportation monitoring, biomedical diagnostics, materials science or chemical process monitoring, aircraft or detector maintenance, and environmental monitoring.[5,6] Therefore, it is important to design a simultaneous temperature and acoustic impedance sensor which can meet the requirements of electromagnetic interference immunity and efficient detection in a limited space while combining high sensitivity and accuracy.

Forward stimulated Brillouin scattering (FSBS, also known as guided acoustic-wave Brillouin scattering or GAWBS) in optical fibers is a typical third-order nonlinear process based on the interaction between incident light and transverse acoustic waves (TAWs).[7] TAWs can propagate along the fiber cross section in the form of penetrating cladding and are highly sensitive to material or mechanical variations outside the fiber, which in turn affect light waves based on the acousto-optic interactions, thus FSBS has great potential for sensing applications.[8] In addition, thanks to the joint participation of multiple order of TAWs, FSBS possesses unique characteristic of diverse scattering peaks that are not present in backward stimulated Brillouin scattering (BSBS), which makes it more suitable for multi-parameter measurements.[3,9] The resonance frequency distribution and scattering peak linewidths of FSBS are smaller than those of BSBS, and therefore, fiber-optic sensing based on FSBS is able to reduce the cost and improve the accuracy.[10]

The intrinsic resonant frequency of TAWs (also known as the Brillouin frequency shift or BFS), which is essentially the displacement deviation between incident and scattered light, is one of the most important covariates for investigating the FSBS-based sensing capability. The transmission velocity of acoustic waves and the phonon reflection lifetime are highly sensitive to the changes in temperature and acoustic impedance outside the fiber cladding, and this sensitivity can be reflected in the BFSs of TAWs.[7] Simultaneous measurement of temperature and acoustic impedance can be achieved by analyzing the linear frequency shift of multiple scattering peaks. So far, FSBS-based simultaneous sensing of temperature and acoustic impedance has been implemented in large effective area fiber (LEAF),[11] G657 single mode fiber (G657-SMF),[3] and 1060-XP fiber,[4] but due to the nature of SMFs, the nonlinear strengths and FSBS gain coefficients are limited,[12] and thus the response strengths of the scattered peaks (i.e., signal-to-noise ratios, SNRs) and sensitivity are

†Corresponding author. E-mail: zxzhang@njupt.edu.cn

© 2025 Chinese Physical Society and IOP Publishing Ltd. All rights, including for text and data mining, AI training, and similar technologies, are reserved.

relatively low. To the best of our knowledge, a simultaneous temperature and acoustic impedance sensor based on a high response strength of FSBS with both high sensitivity and high accuracy has not been reported.

In this work, a simultaneous temperature and acoustic impedance sensor with high sensitivity and accuracy based on the strong FSBS response in highly nonlinear fiber (HNLF) is proposed and demonstrated. Additionally, higher-order acoustic modes (HOAMs) are used for the simultaneous measurement of temperature and acoustic impedance. The measured highest frequency shift-temperature coefficient is 184.93 kHz/°C, which is 26.8, 7.7, 6.7, 5.3, and 1.4 times higher than those of the reported bare SMF,[13] G657-SMF,[3] bare LEAF,[11] 1060-XP fiber,[4] and thin diameter fiber (TDF),[9] respectively; the highest frequency shift acoustic impedance coefficient is 444.56 kHz/MRayl, which is 6.4, 1.5, and 1.1 times higher than those reported for bare SMF,[15] bare LEAF,[11] and 1060-XP fiber,[4] respectively. The measurement errors for temperature and acoustic impedance were 0.09 °C and 0.009 MRayl, respectively. We believe this temperature and acoustic impedance simultaneous sensor can provide valuable solutions and insights for related fields.

2. Theoretical principle and sensing methods

TAWs originate from the material density fluctuations due to electrostriction effects in optical fibers and are a group of discrete mechanical vibration modes formed by phonons oscillating between the cladding and the outer boundary.[8] Their essence can be considered as elastic mechanical waves propagating along the cross section of a cylindrical waveguide. $R_{0,m}$ and $TR_{2,m}$ are two types of TAWs involved in the GAWBS process, and the former usually has a higher response intensity.[16] Therefore, $TR_{2,m}$ is not considered in this work. For the radial acoustic mode $R_{0,m}$ of an ideal silica fiber, the resonance center frequency ν_m of each order can be expressed as[7]

$$\nu_m = \frac{\gamma_m \cdot V_{\mathrm{L}}}{2\pi r}, \tag{1}$$

where V_{L} is the propagation velocity of the longitudinal acoustic wave, which can be generally assumed to be $V_{\mathrm{L}} \approx 5996$ m/s.[17] r is the radius of the fiber cladding. In fact, V_{L} is not constant and depends on the elastic coefficient of the fiber material, $C_{11}(T)$, and the density, ρ. The former has a linear temperature dependence in the range of 20 °C–870 °C, which allows ν_m to be used as a tool of temperature detections.[9] γ_m denotes the eigenvalue of the m-th-order acoustic modes,[18,19] which is determined by the elastic wave equation at the fiber-fluid interface boundary condition and is affected by the acoustic impedance of the fluid medium outside the fiber cladding, Z.[11] The relationship between V_{L} and γ_m as affected by T and Z can be simply expressed as[9]

$$V_{\mathrm{L}} = \sqrt{\frac{C_{11}(T)}{\rho}} = \sqrt{\frac{C_{11}(0) + \dfrac{s}{\exp(\theta_{\mathrm{E}}/T) - 1}}{\rho}}, \tag{2}$$

$$\mathrm{Det}\left\{b_{ij}\left[\gamma_m(Z)\right]\right\} = 0, \tag{3}$$

where $C_{11}(0)$ is the elastic coefficient at 0 K, θ_{E} is the Einstein temperature, and s is a constant. The above quantities are generally assumed to be 77.992 GPa, 420 K, and 6.45×10^9 in silicon fiber, respectively.[9] b is the determinant element. In addition, according to Refs. [4,20], V_{L} and the acoustic impedance of the surrounding medium can also have an approximately linear relationship; as Z in the environment increases, V_{L} increases accordingly. In summary, to visualize that ν_m is a function over T and Z, equation (1) can be rewritten as

$$\nu_m(T,Z) = \gamma_m(Z) \cdot \frac{V_{\mathrm{L}}(T,Z)}{2\pi r}. \tag{4}$$

Several previous works have shown that the resonance frequency of the scattering peaks increases or decreases linearly as a function of T or Z.[3,4,11] By demodulating the spectrum and fitting the scattering peaks, the frequency shift-temperature coefficients C_{ν_T} and the frequency shift-acoustic impedance coefficients C_{ν_Z} can be obtained. For simultaneous measurements, the methodology of Refs. [4,18] is used in this work. By choosing a particular combination of acoustic modes (noted as $R_{0,x}$ and $R_{0,y}$), their resonance center frequencies ν_x and ν_y can be expressed as[4,18,21]

$$\nu_x = \nu_{x_0} + C_{\nu_T_x} \cdot \Delta T + C_{\nu_Z_x} \cdot \Delta Z, \tag{5}$$

$$\nu_y = \nu_{y_0} + C_{\nu_T_y} \cdot \Delta T + C_{\nu_Z_y} \cdot \Delta Z, \tag{6}$$

where ν_{x_0} and ν_{y_0} are the center frequencies of $R_{0,x}$ and $R_{0,y}$ in the initial state; $C_{\nu_T_x}$ and $C_{\nu_Z_x}$ are the frequency shift-temperature coefficient and the frequency shift-acoustic impedance coefficient of $R_{0,x}$, respectively, and the same applies to $C_{\nu_T_y}$ and $C_{\nu_Z_y}$. ΔT and ΔZ refer to the variations in temperature and acoustic impedance, respectively, which can be introduced by Eqs. (5) and (6)[4,18]

$$\begin{bmatrix} \Delta T \\ \Delta Z \end{bmatrix} = \begin{bmatrix} C_{\nu_T_x} & C_{\nu_Z_x} \\ C_{\nu_T_y} & C_{\nu_Z_y} \end{bmatrix}^{-1} \cdot \begin{bmatrix} \Delta\nu_x \\ \Delta\nu_y \end{bmatrix}, \tag{7}$$

where $\Delta\nu_x$ and $\Delta\nu_y$ are the variations in the center frequencies of $R_{0,x}$ and $R_{0,y}$ due to simultaneous changes in T and Z, respectively. Therefore, ΔT and ΔZ can be derived by measuring the center frequency shift of $R_{0,x}$ and $R_{0,y}$. Similarly, the measurement errors δT and δZ (i.e., the theoretical measurement accuracy) can be given by the following equation:[4,18]

$$\begin{bmatrix} \delta T \\ \delta Z \end{bmatrix} = \begin{bmatrix} C_{\nu_T_x} & C_{\nu_Z_x} \\ C_{\nu_T_y} & C_{\nu_Z_y} \end{bmatrix}^{-1} \cdot \begin{bmatrix} \delta\nu_x \\ \delta\nu_y \end{bmatrix}, \tag{8}$$

where $\delta\nu_x$ and $\delta\nu_y$ are the measurement errors of center frequency for $R_{0,x}$ and $R_{0,y}$, respectively. Note that the actual measurement error is given by the difference between $\Delta T/\Delta Z$

measured in Eq. (7) and the actual variation, and may be different from ΔT and ΔZ. This is due to the fact that δv_x and δv_y are obtained from multiple measurements of the resonance frequency of the scattering peaks at a given steady state and calculation of the standard deviation,[3,4,18] which lacks ergodicity. However, equation (8) can still be used as one of the criteria for screening the ideal mode combination. The selected peaks should not only have high sensitivity, but also δT and δZ should be as small as possible.

In this work, HOAMs are defined as the acoustic modes whose resonance frequencies are higher than 1.1 GHz. The temperature and acoustic impedance responses of the above modes are analyzed. Due to the nonlinearity of the HNLF, its FSBS gain coefficient can be higher than that of the SMF under same conditions, and more HOAMs can be excited in the high-frequency band;[12] the acousto-optic interactions in HNLF improve the responsiveness of the TAWs to changes in the external parameters while diversifying the selection of the sensing peaks compared to the SMF. In addition, under a given resolution bandwidth (RBW), the HOAMs have relatively regular and stable scattering peak waveforms, which helps to obtain the value of the resonant frequency v_m more accurately by Lorentzian fitting, and thus improves the accuracy of the frequency shift measurement. It can also be seen from Eq. (4) that the amplitude of the resonance frequency shift tends to increase stepwise when the external parameter changes,[7,9–11] so the HOAMs have relatively stronger measurement sensitivity.

3. Experimental setup and analysis of HOAMs

The experimental setup of the sensor is shown in Fig. 1, where a Sagnac interferometer structure is used to demodulate FSBS in the HNLF. The tunable laser source (YOKOGAWA, AQ2200-136) outputs continuously pump light at a wavelength of 1554.00 nm, which is amplified by an erbium-doped fiber amplifier (EDFA) and then passes through the isolator (ISO) into the Sagnac loop. A 20-m-long uncoated HNLF is used as the fiber under test (FUT), which is connected to a polarization controller (PC) and a 2×2 optical coupler (OC). The pump light passes through the OC and then propagates in two directions, exciting the GAWBS in the FUT firstly. TAWs are generated by the electrostriction effect and then apply phase modulation to the light waves by the elastic-optical effect. Interference occurs after the two beams meet again at the OC, when the phase modulation induced by the TAWs is converted into intensity modulation and received by a 40 GHz photodetector (PD). Finally, the electrical signal is sent to an electrical spectrum analyzer (ESA) to demodulate the frequency domain signal.

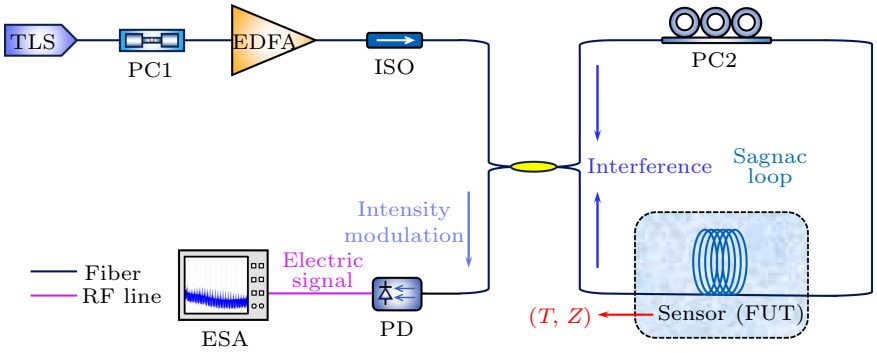


Fig. 1. Experimental setup for the temperature and acoustic impedance simultaneous sensor. TLS: tunable laser source, PC: polarization controller, EDFA: erbium-doped fiber amplifier, ISO: isolator, OC: optical coupler, FUT: fiber under test, PD: photodetector, ESA: electrical spectrum analyzer.

The cladding diameter of the HNLF used in the experiments is 120.5 μm, with a nonlinear coefficient $\geq$ 10 $W^{-1}{\cdot}km^{-1}$ and an attenuation coefficient $\leq$ 1.5 dB/km. The cladding diameter of the other connecting fibers is 125 μm. The coating layer of the FUT was removed by glue remover. the insertion loss can be negligible due to the small diameter difference.[17] Figure 2 shows the measured FSBS spectrum of the 20-m-long uncoated HNLF over a spectral width of 0–1.9 GHz. In the case of the limited phase cumulative intensity of acousto–optic interaction due to the fiber length of 20 m, the scattering peak intensity of the HNLF is higher than that of various SMFs with similar length.[12] In addition, as the frequency increases (above 1 GHz), the TAWs still maintain certain response intensity, while TAWs excited in various types of SMFs are very weak at 600 MHz–800 MHz.[3,4,11,18] The unique advantages of the HNLF can provide the sensor with ideal sensitivity and more choice of sensing parameters.

The red box and inset are the HOAMs in the frequency band from 1.1 GHz to 1.9 GHz, corresponding to the 23rd to the 38th order modes. It can be seen that, compared with the scattering peaks with resonance frequencies below 1.1 GHz, the waveforms of the HOAMs are relatively more regular and stable, with almost no overlap with $TR_{2,m}$, resulting in smaller deviations from the Lorentzian fitting curves and smaller fluctuations in multiple measurements of the center frequency un-

der the steady state. This also helps to improve the measurement accuracy. Therefore, HOAMs are more advantageous when it is necessary to obtain the frequency standard deviation of a specific scattering peak.

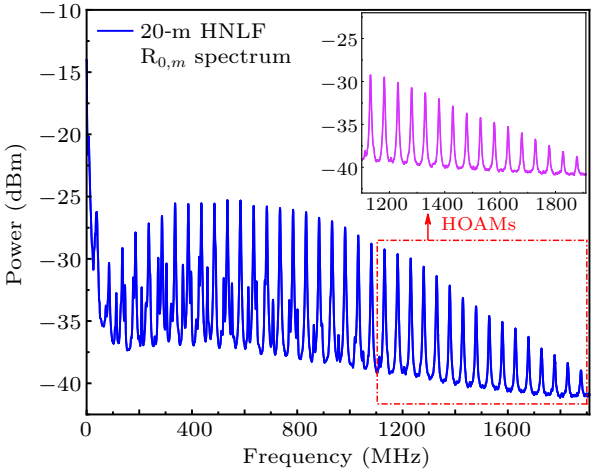


Fig. 2. Measured FSBS gain spectrum of the 20-m-long uncoated HNLF at room temperature in the frequency band of 0–1.9 GHz. The scattering peaks in the inset indicate the HOAMs ($R_{0,23}$ to $R_{0,38}$).

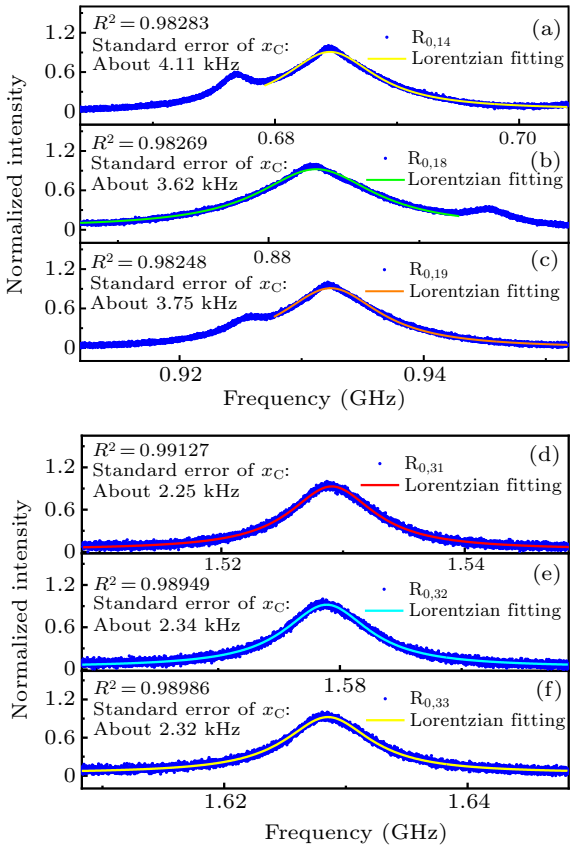


Fig. 3. Three relatively low-order modes and HOAMs for comparison.

We also measured the scattering peaks of several modes (including HOAMs) to briefly verify this conclusion. The spectra of the three HOAMs ($R_{0,31}$, $R_{0,32}$, and $R_{0,33}$) and three relatively low-order modes ($R_{0,14}$, $R_{0,18}$, and $R_{0,19}$) were measured, as shown in Fig. 3. Both RBW and VBW are the same during the measurement. Affected by waveform irregularity and overlap with TR modes, the fitting effect of the scattering peaks and the center frequency fitting errors in panels (a)–(c) are not as good as those of the HOAMs in panels (e)–(f). The waveforms of HOAMs are obviously more regular, and their fitting curves are closer to the actual waveforms, so the measurement error is relatively small. Combined with high sensitivity, HOAMs are a preferable choice for sensing.

4. Experiment to test the sensing performance

To use the FUT for simultaneous measurement of temperature and acoustic impedance, the responsivity of the resonant center frequencies to T and Z should be obtained firstly. Then, δT and δZ of each mode combination can be derived from the frequency standard deviations of scattering peaks at steady state, then the optimal ($R_{0,x}$, $R_{0,y}$) is selected. Finally, the outer state of FUT is set to switch from (T_1, Z_1) to (T_2, Z_2) to test the measurement accuracy of the sensor. $R_{0,32}$ will be used as the example in the sensitivity measurement section below. In addition, the effects of T and Z on the linewidth of the scattering peak are not considered in the measurements.

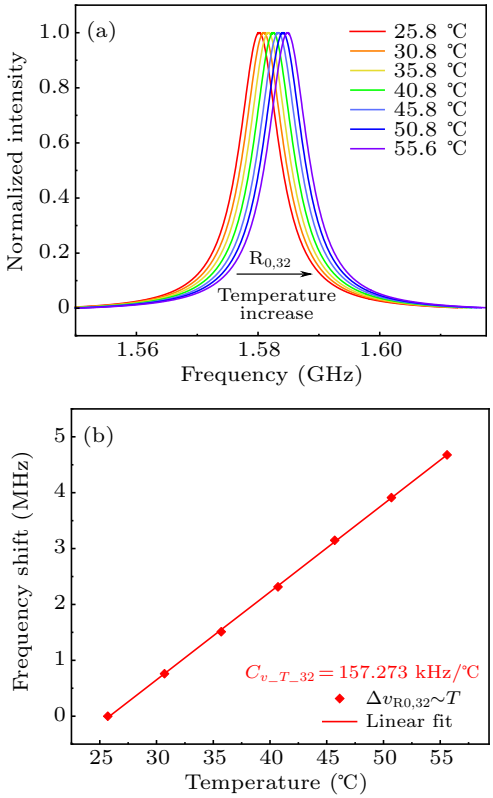


Fig. 4. (a) Measured center frequency variation of $R_{0,32}$ at different temperatures. (b) Frequency shift-temperature coefficient of $R_{0,32}$.

Firstly, the FUT was placed in a thermostatic purified water bath and the temperature was set to increase from 25 °C to 55 °C with intervals of 5 °C. Each state was maintained for 30 minutes to ensure temperature stabilization. It was found that the actual temperature of the liquid deviated from the setting, so the frequency shift measurements were based on the actual temperature. The frequency shifts of the peaks from $R_{0,23}$ to $R_{0,38}$ were measured during the heating process, and

the frequency shift patterns of $R_{0,32}$ are shown in Figs. 4(a) and 4(b). All scattering peaks are subjected to a normalized Lorentzian fit. The initial reference state is set to 25.8 °C. It can be seen that the resonance frequency of $R_{0,32}$ shows a good linear shift as the ambient temperature outside the cladding increase, and the measured frequency shift-temperature coefficient is 157.273 kHz/°C. Although the temperature sensitivity of $R_{0,32}$ is not the highest, it is still 1.2 times higher than the temperature sensitivities of the TDFs mentioned in Section 1.

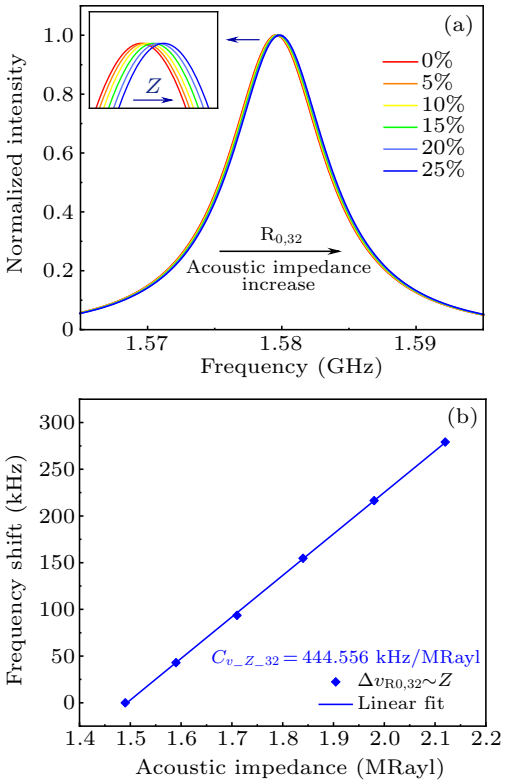


Fig. 5. (a) Center frequency variation of $R_{0,32}$ measured at different solution concentrations. (b) Frequency shift-acoustic impedance coefficient of $R_{0,32}$.

Next, the FUT was immersed into NaCl solutions at concentrations of 0% (pure water), 5%, 10%, 15%, 20%, and 25% to simulate acoustic impedance changes in the environment outside the cladding. The acoustic impedance of the NaCl solutions at the above concentrations at room temperature of 22 °C is given in the Refs. [3,20]. The amount of solution was controlled and the solution temperature was kept constant. The resonant frequency variations from $R_{0,23}$ to $R_{0,32}$ at different concentrations were measured and the frequency shift-acoustic impedance coefficients were calculated by linear fitting using the center frequency at 0% concentration as the initial reference point. The results of $R_{0,32}$ is shown in Figs. 5(a) and 5(b). It should be noted that the frequency shift characteristics of $R_{0,33}$ to $R_{0,38}$ were not measured due to the fact that these peaks have low original response strength and the increase in the acoustic ambient impedance outside the cladding weakens the SNR of the peaks,[11] making it difficult to detect resonance frequencies. As can be seen in Fig. 5, there is a linear relationship between the frequency shift and the change in acoustic impedance; by fitting, the frequency shift-acoustic impedance coefficient was calculated to be 444.556 kHz/MRayl for $R_{0,32}$.

The measured C_{v_T} and C_{v_Z} for the other acoustic modes are shown in Fig. 6(a). It can be seen that the temperature sensitivity shows a steady stepwise increasing trend; from the linear fit, a single step increase in C_{v_T} is calculated to be about 4.895 kHz/°C. The acoustic impedance sensitivity corresponds to blue curve also shows an increasing trend. As mentioned above, C_{v_Z} of $R_{0,33}$ to $R_{0,38}$ was not measured due to the low intensity of the scattering peaks; therefore, HOAMs from $R_{0,33}$ to $R_{0,38}$ were not considered for the selection of mode combinations.

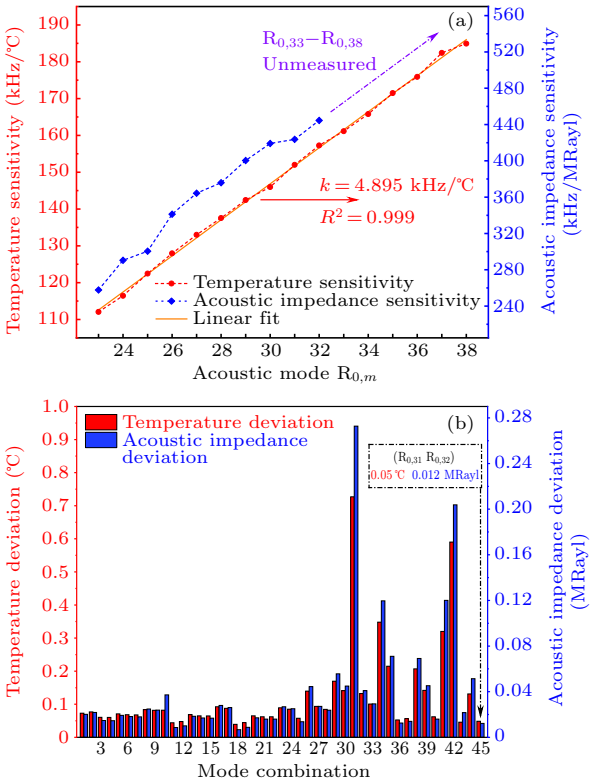


Fig. 6. (a) C_{v_T} and C_{v_Z} of HOAMs, (b) δT and δZ of 45 mode combinations derived from the standard deviations of center frequency from $R_{0,23}$ to $R_{0,32}$

We have already measured the C_{v_T} and C_{v_Z} of HOAMs and identified the scattering peaks involved in the screening of mode combinations, i.e., $R_{0,23}$ to $R_{0,32}$. These 10 modes can be paired together to produce 45 groups of mode combinations. For easy identification, the combinations are numbered in the order of permutation, i.e., from combinations ($R_{0,23}$, $R_{0,24}$) to ($R_{0,31}$, $R_{0,32}$) corresponding to No. 1–No. 45. To determine the best combination, δT and δZ must be obtained at steady state and examined in conjunction with the sensitivities. Therefore, the FUT was immersed in pure water with temperature of 22 °C, and the spectra from $R_{0,23}$ to $R_{0,32}$

were measured eight times. δv of each mode was obtained by Lorentzian fitting, and δT and δZ were calculated by Eq. (8). The results are shown in Fig. 6(b). By combining the sensitivities in Fig. 6(a), the 45th combination, i.e., ($R_{0,31}$, $R_{0,32}$), is finally selected. The measured δv_{31} and δv_{32} are 2206.87 Hz and 2207.47 Hz, respectively, from which the δT and δZ of ($R_{0,31}$, $R_{0,32}$) are calculated to be 0.05 °C and 0.012 MRayl, respectively.

To verify the feasibility of the selected combination, a proof-of-concept experiment was performed under different temperature and acoustic impedance conditions. First, the FUT was placed in pure water (i.e., 0% NaCl solution) at a temperature stabilized at 28.8 °C, which was recorded as state 1; then, the FUT was immersed in 15% NaCl solution and its temperature was maintained at 19.8 °C, which was recorded as state 2. During the state switching process, all other variables except temperature and acoustic impedance were kept constant (including water pressure, bending loss, and optical power, etc.). Figures 7(a)–7(d) represent the spectra of $R_{0,31}$ and $R_{0,32}$ with RBW set to 2 kHz. According to the Lorentz fit, the v_{31_1} and v_{32_1} of state 1 are 1530.795 MHz and 1580.627 MHz, respectively; the v_{31_1} and v_{32_1} of state 2 are 1529.566 MHz and 1579.357 MHz, respectively.

State 1 and state 2 are considered as the initial state and the final state, respectively. Substituting Δv_{31} and Δv_{32} into Eq. (7) and combining with the corresponding sensitivities gives $\Delta T = 9.09$ °C and $\Delta Z = 0.359$ MRayl. In fact, during the state switching process, the change in temperature is 9 °C and the change in acoustic impedance is 0.350 MRayl.[25] Therefore, the accuracies of the temperature and acoustic impedance measurements are obtained to be 0.09 °C and 0.009 MRayl, respectively. Compared with the $\delta T = 0.05$ °C and $\delta Z =$ 0.012 MRayl calculated in the previous section, the slight deviation maybe due to the calibration error of the sensitivity in Eq. (7).[3,4]

We compared this work with several fiber-optic sensors in related fields, as shown in Table 1. The sensitivity refers to the frequency shift coefficient. It can be seen that HNLF has a more advantageous overall performance and achieves a desirable measurement accuracy of 0.09 °C and 0.009 MRayl. Although C_{v_Z} is not as good as Ref. [3], the C_{v_T} is 7.7 times better and has a favorable accuracy. The sensor is also quite competitive in terms of measurement time and measurement range.[11] In terms of cost for an optical system, our experimental setup has relatively low requirements for the instruments; The Sagnac interferometer, one of the simplest FSBS demodulation schemes, is also of low system complexity.

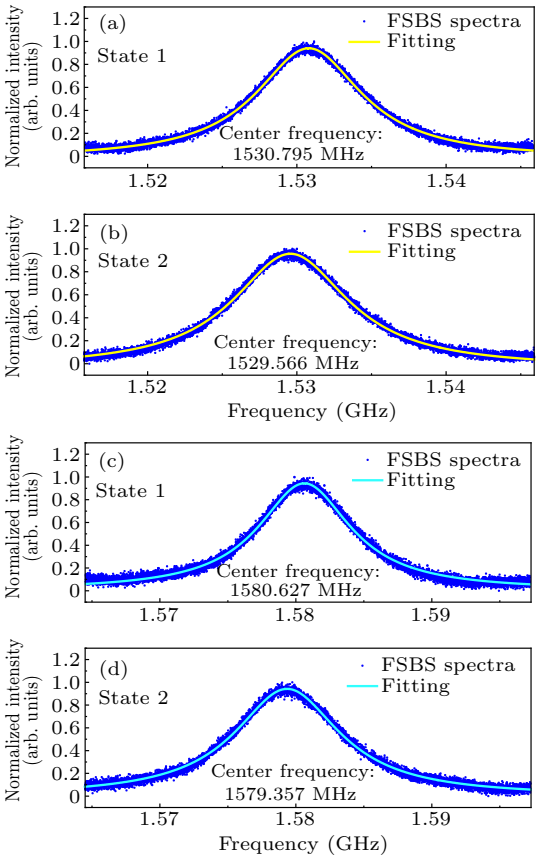


Fig. 7. (a)–(b) FSBS spectra of $R_{0,31}$ in state 1 and state 2, (c)–(d) FSBS spectra of $R_{0,32}$ in state 1 and state 2.

Table 1. Comparisons of several fiber-optic sensors involving temperature or acoustic impedance.

Refs.	Principle	Temperature sensitivity (v_m)	Acoustic impedance sensitivity (v_m)	Temperature accuracy (°C)	Acoustic impedance accuracy (MRayl)
[23]	Raman scattering	–	–	5	–
[25]	OFDR	1.22 MHz/°C	–	1.2	–
[26,27]	MZI	–	–	0.8	–
[28]	BSBS	1.1 MHz/°C	–	0.71	–
[29]	FSBS	–	–	0.65	–
[30]	FSBS	43.5 kHz/°C	–	0.2	–
[9]	FSBS	130.38 kHz/°C	–	0.15	–
[22]	FSBS	–	–	–	0.069
[32]	FSBS	–	–	–	0.15
[17]	FSBS	–	–	–	0.031
[3]	FSBS	24 kHz/°C	1.66 MHz/MRayl	0.17	0.007
[11]	FSBS	27.6 kHz/°C	302 kHz/MRayl	0.1	0.006
[4]	FSBS	35.13 kHz/°C	405 kHz/MRayl	0.13	0.006
This work	**FSBS**	**184.93 kHz/°C**	**444.56 kHz/MRayl**	**0.09**	**0.009**

Notes: OFDR: optical frequency-domain reflectometry, MZI: Mach–Zehnder interferometer.

In addition, our work has some advantages over studies that also use HOAMs.[33] The relatively shorter fiber improves the size, weight, and cost of the sensor; the higher overall intensity of the scattering peaks has the advantage that HOAMs are more selective and have higher overall order, which provides better sensitivity and less overlap with TR modes, resulting in a more regular and rounded waveform which is easier to fit. Avoiding the relatively weak response of TR modes also favors high sensitivity and accuracy of detection.

It should be noted that HOAMs themselves can be a source of potential errors. Although our experiments achieved high-accuracy measurement with HOAMs, the demodulation of HOAMs places certain requirements on the system loss and FSBS gain of the FUT. If the scattering peaks in the high-frequency domain are too weak, it may lead to the deviation of the frequency measurement. In addition, Lorentzian fitting with high R^2 values also requires proper resolution bandwidth (RBW) and visual bandwidth (VBW). Inappropriate bandwidth settings may cause unwanted clutter and burr on the scattering peaks and affect the waveform, and thus the center frequency measurement error of the fitted curves may be large.

5. Conclusion

In this work, a simultaneous temperature and acoustic impedance sensor with high sensitivity and accuracy based on the FSBS in HNLF is proposed and demonstrated, and the resonance center frequencies of HOAMs are utilized to achieve single or dual-parameter sensing of temperature and acoustic impedance. Using a 20-m-long uncoated HNLF as the FUT combined with Sagnac interferometer, the highest frequency shift-temperature coefficient and frequency shift-acoustic impedance coefficient were measured to be 184.93 kHz/°C and 444.56 kHz/MRayl, respectively; in the proof-of-concept experiment using $R_{0,31}$ and $R_{0,32}$, the sensor was measured to have a sensing accuracy of 0.09 °C and 0.009 MRayl.

In subsequent studies, the sensor can be combined with the distributed fiber-optic sensing and high compactness or high spatial resolution detection schemes such as opto-mechanical time-domain reflectometry (OMTDR),[31] opto-mechanical time-domain analysis (OMTDA),[32] fiber Bragg gratings (FBGs),[24] and frequency-division multiplexing (FDM) schemes.[17] Additionally, since FSBS is rarely studied in other sensing fields involving acoustical, optical, electrical, thermal, and magnetic parameters (e.g., acoustic wave intensity, light intensity, current–voltage, magnetic field, etc.), this may also be one of the optimization directions of FSBS-based fiber-optic sensing applications. In conclusion, we still believe that this work has a remarkable potential for applications in the field of high-sensitivity and high-precision temperature or acoustic impedance sensing.

Data availability statement

The data that support the findings of this study are openly available in Science Data Bank at https://doi.org/10.57760/sciencedb.j00113.00229.

References

[1] Qiu L Q, Zhu Z D, Li T F, Zhou D W and Dong Y K 2021 *IEEE Sens. J.* **21** 6209
[2] Catalano E, Vallifuoco R, Zeni L and Minardo A 2022 *IEEE Sens. J.* **22** 6601
[3] Liang L L, Zhang Z L, Zhang W J, Peng J Q, Li X H and Lu Y G 2023 *IEEE Photon. Technol. Lett.* **35** 1151
[4] Liu P K, Lu Y G, Zhang W J and Zhu M 2024 *Opt. Commun.* **563** 130571
[5] Hoffman L, Müller M S, Krämer S, Giebel M, Schwotzer G and Wieduwilt T 2007 *Estonian J. Eng* **13** 363
[6] Zorebski E, Zorebski M and Dzida M 2016 *Arch. Acoust. Q* **41** 59
[7] Shelby R M, Levenson M D and Bayer P W 1985 *Phys. Rev. B* **31** 5244
[8] Li T F, Ba D X, Zhou D W, Ren Y L, Chen C, Zhang H Y and Dong Y K 2022 *Opto-Electron. Eng.* **49** 220021
[9] Zhang L, Wang H, Li Y C, Gao S, Zhu M S, Wei H M, Pang F F and Wang T Y 2024 *Opt. Express* **32** 586
[10] Yang G J, Zeng K Y, Wang L, Tang M and Liu D M 2023 *Opt. Lett.* **48** 3611
[11] Zhang Z L, Lu Y G, Peng J Q and Ji Z Y 2021 *Opt. Lett.* **46** 1776
[12] Zeng K Y, Yang G J, Xu Z Y, Song L, Wang L, Tang M and Liu D M 2023 *Opt. Express* **31** 8595
[13] Fu Y X, Fan X Y, Wang B and He Z Y 2018 *Asia Commun. Photon. Conf.*, 2018, Hangzhou, China, 2018, p. 1
[14] Zhang W J, Lu Y G and He C J 2023 *IEEE Sens. J.* **23** 27361
[15] Hayashi N, Mizuno Y, Nakamura K, Set S Y and Yamashita S 2017 *Opt. Express* **25** 2239
[16] Cao M, Huang L, Tang M, Mi Y A, Jian W, Ren W H and Ren G B 2020 *J. Lightw. Technol.* **38** 6911
[17] Zheng Z, Li Z Y, Fu X L, Wang L X and Wang H H 2020 *Opt. Lett.* **45** 4523
[18] Li X H, Lu Y G and Zhang Z L 2023 *J. Lightw. Technol.* **41** 5130
[19] Shelby R M, Levenson M and Bayer P 1985 *Phys. Rev. Lett.* **54** 939
[20] Puttmer A, Hauptmann P and Henning B 2000 *IEEE Trans. Son. Ultrason.* **47** 85
[21] Zhang Z L, Lu Y G, Tanaka Y, Peng J Q and Zhuang Z K 2021 *Appl. Phys. Exp.* **14** 042004
[22] Chow D M and Thévenaz L 2018 *Opt. Lett.* **43** 5467
[23] Silva M E, Barros T and Alves H 2021 *IEEE Sens. J.* **21** 1527
[24] Tommasi F D, D'Alvia L, Massaroni C, Presti D, Carassiti M and Prete Z D 2023 *IEEE Trans. Instrum. Meas.* **72** 4007310
[25] Zhou D P, Li W H, Chen L and Bao X Y 2013 *Sensors* **13** 1836
[26] Geng Y F, Li X J, Tan X L, Deng Y L and Yu Y Q 2011 *IEEE Sens. J.* **11** 2891
[27] Zhou J T, Liao C R, Wang Y P, Yin G L, Zhong X Y, Yang K M, Sun B, Wang G J and Li Z Y 2014 *Opt. Express* **22** 1680
[28] Bai Q, Xue B, Gu H, Wang D, Wang Y, Zhang M J, Jin B Q and Wang Y C 2019 *IEEE Photon. Technol. Lett.* **31** 283
[29] Antman Y, London Y and Zadok A 2015 *Proc. 24th Int. Conf. Opt. Fiber Sensors*, 2015, Lausanne, Switzerland, p. 696
[30] Sánchez L A, Díez A, Cruz J L and Andrés M V 2022 *Opt. Express* **30** 14384
[31] Bashan G, Diamandi H H, London Y, Preter E and Zadok A 2018 *Nat. Commun.* **9** 2991
[32] Pang C, Hua Z J, Zhou D W, Zhang H Y, Chen L, Bao X Y and Dong Y K 2020 *Optica* **7** 176
[33] Zhu M, Lu Y G, Zhang Z L, Liu P K and Zhang W J 2024 *Opt. Fiber Technol.* **84** 103741